ISSN 0021-3640, JETP Letters, 2023, Vol. 118, No. 7, pp. 495–501. © The Author(s), 2023. This article is an open access publication.
Russian Text © The Author(s), 2023, published in Pis'ma v Zhurnal Eksperimental'noi i Teoreticheskoi Fiziki, 2023, Vol. 118, No. 7, pp. 506–512.

CONDENSED MATTER

Giant Planar Hall Effect in an Ultra-Pure Mercury Selenide Single Crystal Sample

S. B. Bobin[a, *] and A. T. Lonchakov[a]

[a] *Mikheev Institute of Metal Physics, Ural Branch, Russian Academy of Sciences, Yekaterinburg, 620108 Russia*

**e-mail: bobin@imp.uran.ru*

Received August 7, 2023; revised August 22, 2023; accepted August 22, 2023

A giant planar Hall effect with an amplitude of about 50 mΩ cm at a temperature of $T = 80$ K in a magnetic field of 10 T has been detected in an ultra-pure HgSe single crystal sample with an electron density of 5.5×10^{15} cm^{-3}. Its oscillating dependence on the rotation angle of the sample in various magnetic fields has been determined. Attributes (oscillation period, positions of extrema, correlation between the amplitudes of planar Hall and planar longitudinal magnetoresistance) indicate that the planar Hall effect in this nonmagnetic gapless semimetal with an isotropic Fermi surface originates from the chiral anomaly. This is a solid argument for the topological nature of the electronic spectrum of HgSe.

DOI: 10.1134/S0021364023602658

INTRODUCTION

The planar Hall effect (PHE) was discovered as a new galvanomagnetic phenomenon in 1954 in *n*- and *p*-Ge crystals [1] and was explained by the anisotropy of the magnetoresistance (MR), which is due to the anisotropy of the Fermi surface and the relaxation time. Experimentally, the PHE is discovered as the emergent transverse potential difference in case of applied magnetic and electrical fields lie in a single plane. In addition, the angle between the magnetic and electrical fields should differ from 0 (π) and $\pi/2$ ($3\pi/2$), which is ensured by rotating the sample in the magnetic field. This feature distinguishes the PHE from a conventional Hall effect, which requires a nonzero magnetic field component perpendicular to the plane of the sample (and, correspondingly, to the electrical current). Later, the PHE was observed in ferromagnetic systems such as Fe_3GeTe_2 [2], $Co_{60}Fe_{20}B_{20}$ [3], $Sr_4Ru_3O_{10}$ [4], and $La_{2/3}Ca_{1/3}MnO_3$ [5], epitaxial (Ga, Mn)As structures [6], besides nonmagnetic materials with the anisotropy of the orbital MR (also known as the classical MR induced by the Lorentz force). The commonly accepted origin of the PHE in such systems is a change in the probability of the spin–orbit scattering under the rotation of the in-plane magnetization following the magnetic field with respect to the electrical field [7]. Studies of the PHE in ferromagnetic materials demonstrated that these materials can be applied as the basics for a new type of magnetic random access memory [8]. Furthermore, the PHE in ferromagnetic materials can be used to develop magnetic sensors for nanotesla detection with a resolution better than 10 nT [9].

Interest in the PHE has increased significantly in recent years after the discovery of topological Dirac [10–12] and Weyl [13–17] semimetals. The authors of theoretical works [18, 19] attributed the PHE in these materials to the inherent chiral anomaly, i.e., nonconservation of the number of Weyl fermions with opposite chirality in parallel electrical and magnetic fields [20]. According to [20], the chiral anomaly is due to the breaking of the fundamental chiral symmetry of massless fermions. This was first discovered in the experiment with an A-phase of superfluid ^{3}He, which contains Weyl fermions [21]. It follows that the PHE can be used as a specific test for the chiral anomaly and, thereby, Weyl nodes with opposite chirality in isotropic nonmagnetic solids. It appeared that the PHE is observed according to the theoretical predictions [18, 19] either in Dirac semimetals $ZrTe_{5-\delta}$ [22], $PdTe_2$ [23, 24], Cd_3As_2 [25, 26], $ValI_3$ [27], $PtTe_2$ [28] or Weyl semimetals Na_3Bi [29], CdPtBi [29, 30], T_d-$MoTe_2$ [31], WTe_2 [32], and TaAs [33]. At the same time, the anisotropy of the orbital MR was considered as the origin for the PHE in Dirac semimetals $NiTe_2$ [34] and $PtSe_2$ [35].

In addition to the PHE, the chiral magnetic effect also occurs in topological semimetals due to the chiral anomaly [36–40]. This effect consists in the generation of the additional current induced by the chiral imbalance, which in turn emerges in a magnetic field parallel to an electrical field. This additional (chiral) current is always aligned along the main current; i.e., the chiral magnetic effect is of a longitudinal type unlike the transverse PHE. Experimentally, the chiral magnetic effect manifests itself as a positive contribu-

tion to conductivity, which is quadratic in the magnetic field. It is believed that the observation of the chiral magnetic effect in topological semimetals is a necessary condition for the observation of the chiral anomaly-induced PHE.

Recently, we studied a positive longitudinal magnetoconductivity induced by the chiral magnetic effect in mercury selenide samples with a low electron concentration n_e of (0.55–17) × 10^{16} cm^{-3} [41]. We also revealed some features of the longitudinal and transverse MR [42], nontrivial Berry phase, and electronic topological Lifshitz transition triggered by the shift in the Fermi energy [43], and an unconventional transverse quantum effect in the longitudinal magnetic field [44] in HgSe. All these results imply that HgSe contains not only the trivial gapless phase but also the electronic topological phase of an inversion-breaking Weyl semimetal. Consequently, the PHE is of fundamental importance for the verification of the topological nature of HgSe. The aim of the present work was to reveal the chiral anomaly-induced PHE in nonmagnetic mercury selenide with a nearly spherical Fermi surface [45, 46].

EXPERIMENT

In this work, we investigated one of the HgSe samples, which was previously studied for the chiral magnetic effect [41]. Its uniqueness lies in its purity, since it has the record low electron density n_e = 5.5 × 10^{15} cm^{-3} and the record high electron mobility 3.4 × 10^5 $cm^2/(V\ s)$ for HgSe. The sample was prepared more than four decades ago from a homogeneous part of an ingot grown by the Bridgman method and was annealed in Se vapor. The subsequent long-term passive annealing should obviously had lead to a significant decrease in the number of interstitial mercury atoms and vacancies in the anion sublattice (donor defects in HgSe [46]), thus ensuring such a low electron density. The choice of a sample with a very low Fermi energy is of primary importance for the accomplishment of the pronounced chirality, allowing HgSe to approach an ideal Weyl semimetal. The main electronic and geometrical parameters of the sample having rectangular parallelepiped shape are summarized in [41]. We used a standard for HgSe procedure of the sample surface etching and the preparation of ohmic contacts, which is described in [42]. The crystal structure of HgSe was studied in [43]. The magnetotransport properties were investigated at temperatures of T = 80 and 150 K by the standard four-probe method in a magnetic field up to 12 T using the equipment of the Collaborative Access Center "Testing Center of Nanotechnology and Advanced Materials" of the M.N. Mikheev Institute of Metal Physics of Ural Branch of Russian Academy of Sciences. The sample was rotated in the angle range of 0 to π in a magnetic field with two opposite directions, which is equivalent to the rotation of the sample in the angle range of 0 to 2π. Both transverse MR ρ_{xy} and longitudinal MR ρ_{xx} were measured as a function of the rotation angle α. They are determined by the transverse and longitudinal voltages V_{xy} and V_{xx} each measured from two pairs of contacts (1–3), (2–4) and (1–2), (3–4), respectively (Fig. 1a). The experiment showed that the difference between V_{xy} and V_{xx} is insignificant for different pairs of contacts. Therefore, ρ_{xy} and ρ_{xx} values presented below were obtained by averaging over two pairs of contacts. Due to rotator design feature, it was convenient to measure α from the direction perpendicular to the electrical current, as shown in Fig. 1a.

According to the theory [18], the chiral anomaly-induced planar Hall resistance ρ_{xy} and the planar longitudinal MR ρ_{xx} are given by the expressions

$$\rho_{xy} = \Delta\rho_{\text{chiral}}\sin\alpha\cos\alpha, \quad (1)$$

$$\rho_{xx} = \rho_{\perp} - \Delta\rho_{\text{chiral}}\cos^2\alpha, \quad (2)$$

where $\Delta\rho_{\text{chiral}} = \rho_{\perp} - \rho_{\parallel}$ is the chiral anomaly-induced anisotropy of the MR (the amplitude of the PHE), $\rho_{\perp}$ and $\rho_{\parallel}$ are the in-plane MR in the magnetic field **B** perpendicular and parallel to the electrical current **J**, respectively (Fig. 1a). The expression for $\Delta\rho_{\text{chiral}}$ in terms of the chirality-related parameters of the theory is discussed below.

EXPERIMENTAL RESULTS AND DISCUSSION

Before presenting experimental results, we would like to point to two main factors distorting the dependences $\rho_{xy}(\alpha)$ and $\rho_{xx}(\alpha)$. The first factor is the contribution $\delta\rho_{xy}^{\perp}$ to ρ_{xy} from the conventional Hall effect, originating from perpendicular to the XY plane magnetic field component $\delta B_{\perp}$, which is caused by a misalignment in the sample orientation. Since according to Eq. (1) the conventional Hall effect is odd function on a magnetic field, and the PHE is even function on a magnetic field, the contribution $\delta\rho_{xy}^{\perp}$ can be excluded using the standard averaging over the magnetic field direction:

$$\langle\rho_{xy}(B,\alpha)\rangle_B = \frac{\rho_{xy}(+\mathbf{B},\alpha) + \rho_{xy}(-\mathbf{B},\alpha)}{2}. \quad (3)$$

An example of such averaging is presented in Fig. 1b by a solid line for the raw data $\rho_{xy}(\alpha)$ obtained in magnetic fields of +10 and −10 T, which are depicted by circles. The extracted contribution $\delta\rho_{xy}^{\perp}$ is demonstrated by the dashed line. The second factor is the inevitable displacement of Hall contacts with respect to each other during a sample preparation, which is illustrated by dashed rectangles in Fig. 1a. Due to a non-equipotentiality of the Hall contacts, the

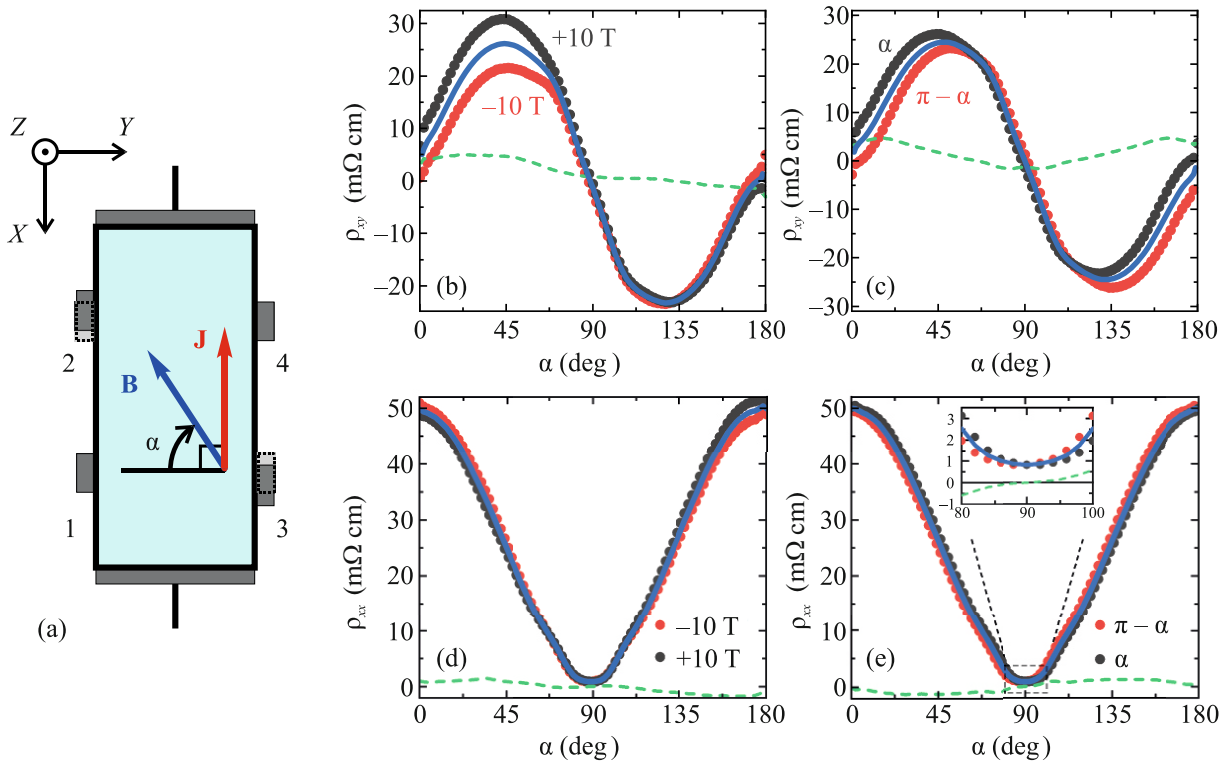

Fig. 1. (Color online) (a) *XY* plane geometry of the PHE study: **B** is the applied magnetic field, α is the angle of magnetic field rotation, and **J** is the electrical current. Gray and dotted rectangle illustrates the actual and the desirable arrangement of Hall contacts, respectively. (b) Angular dependences of the raw planar Hall resistance ρ_{xy} in fields of +10 and −10 T at $T = 80$ K (circles), the planar Hall resistance ρ_{xy} averaged over the direction of the magnetic field (solid line), and odd contribution $\delta\rho^{\perp}_{xy}$ (dashed line). (c) Planar Hall resistance ρ_{xy} averaged over the magnetic field versus the angles α and π–α (circles), the planar Hall resistance ρ_{xy} averaged over α (solid line), and even-angle contribution $\delta\rho^{\parallel}_{xx}$ (dashed line). (d) Angular dependences of the raw planar Hall resistance ρ_{xx} in fields of +10 and −10 T at $T = 80$ K (circles), the planar Hall resistance ρ_{xx} averaged over the direction of the magnetic field (solid line), and odd contribution $\delta\rho^{\perp}_{xy}$ (dashed line). (e) Planar Hall resistance ρ_{xx} averaged over the magnetic field versus the angles α and π–α (circles), the planar Hall resistance ρ_{xx} averaged over α (solid line), and related even-angle contribution $\delta\rho^{\parallel}_{xy}$ (dashed line).

longitudinal MR introduces the contribution $\delta\rho^{\parallel}_{xx}$ to the measured transverse effect. According to Eqs. (1) and (2), ρ_{xy} and ρ_{xx} are the odd and even functions of α, respectively. Therefore, the contribution $\delta\rho^{\parallel}_{xx}$ can be excluded by means of the averaging over an angle as follows:

$$\langle\rho_{xy}(\mathbf{B},\alpha)\rangle_{\alpha} = \frac{\langle\rho_{xy}(\mathbf{B},\alpha)\rangle_{\mathbf{B}} - \langle\rho_{xy}(\mathbf{B},\pi-\alpha)\rangle_{\mathbf{B}}}{2}, \quad (4)$$

where $\langle\rho_{xy}(\mathbf{B},\alpha)\rangle_{\mathbf{B}}$ and $\langle\rho_{xy}(B,\pi-\alpha)\rangle_{B}$ determined using Eq. (3) and are demonstrated by circles in Fig. 1c. The dashed line is the extracted even-angle contribution $\delta\rho^{\parallel}_{xx}(\alpha)$ and the solid line is the finalized dependence $\rho_{xy}(\alpha)$ in the magnetic field of 10 T. The processing of $\rho_{xx}(\alpha)$ data to exclude the contribution $\delta'\rho^{\perp}_{xy}$ originating from $\delta B_{\perp}$ (Fig. 1d) is similar to that of $\rho_{xy}(\alpha)$. In the final, the processing (Fig. 1e) excludes the angle-odd contribution $\delta\rho^{\parallel}_{xy}$ originating from the PHE due to non-equipotentiality.

Thus processed data for $\rho_{xy}(\alpha)$ and $\rho_{xx}(\alpha)$ are presented by circles in Figs. 2a and 2b, respectively. The solid lines represent the fitting of experimental data by Eq. (1) and (2). It can be seen that $\rho_{xy}(\alpha)$ is an oscillating function with a period of π having extrema at $\alpha = \frac{\pi}{4}$ and $\frac{3\pi}{4}$, according to Eq. (1). The function $\rho_{xx}(\alpha)$ also oscillates with the same period, whilst reaching a maximum and a minimum at $\alpha = 0$ and $\frac{\pi}{2}$, respectively. Thus, the phase shift between $\rho_{xy}(\alpha)$ and $\rho_{xx}(\alpha)$ is $\frac{\pi}{4}$. In addition, the right axis in Fig. 2b presents the

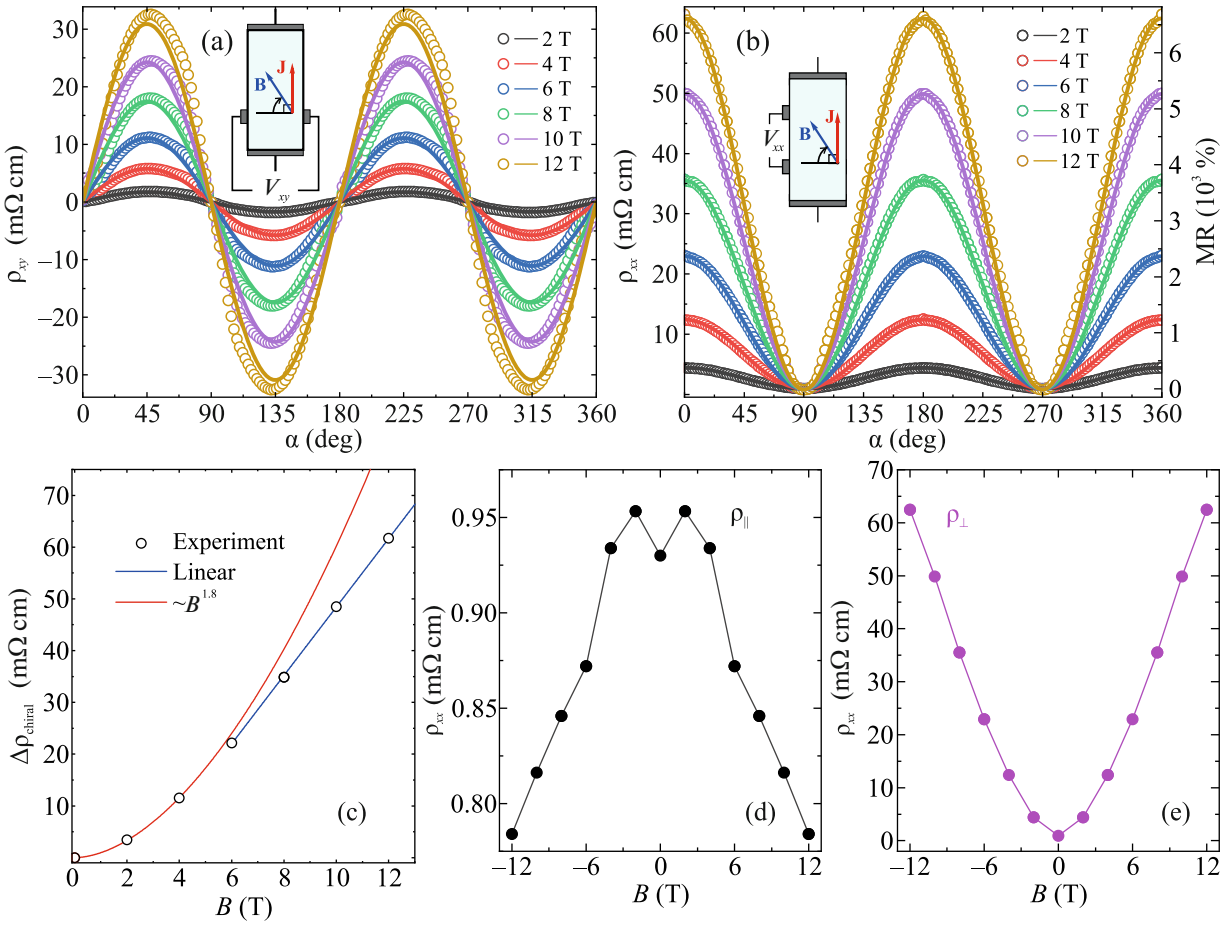

Fig. 2. (Color online) (a) Angular dependences of the planar Hall resistance $\rho_{xy}(\alpha)$ (circles) and its fitting by Eq. (1) (solid lines) in various magnetic fields at $T = 80$ K. The inset shows the transverse voltage V_{xy} measurement sketch. (b) Angular dependence of the planar longitudinal magnetoresistance $\rho_{xx}(\alpha)$ and the normalized MR (circles) and their fitting by Eq. (2) (solid lines) in various magnetic fields at $T = 80$ K. The inset shows the longitudinal voltage V_{xx} measurement sketch. (c) Magnetic field dependence of the PHE amplitude $\Delta\rho_{\text{chiral}}$ (circles) at $T = 80$ K plotted using the fitting data from the panel (a). Red and blue solid lines represent fitting of the data with $B^{1.8}$ power law and a linear function, respectively. (d, e) Magnetic field dependence of the magnetoresistance ρ_{xx} in the magnetic field $\mathbf{B} \parallel \mathbf{J}$ (panel d) and $\mathbf{B} \perp \mathbf{J}$ (panel e).

normalized magnetoresistance $\text{MR} = \dfrac{\rho_{xx}(\alpha, B) - \rho_0}{\rho_0}$ at a fixed magnetic field B, given ρ_0 is a resistivity in zero magnetic field.

To calculate the amplitude of the chiral anomaly-induced PHE in the semiclassical theory [18], the following three characteristic lengths are introduced. The first length is $L_a = \dfrac{D}{\Gamma B}$, where D is the diffusion coefficient of the chiral charge and $\Gamma = \dfrac{e}{2\pi g}$ is the transport coefficient characterizing the chiral anomaly (e is the electron charge and g is the density of states at the Fermi level); L_a^{-1} quantifies the strength of the chiral anomaly induced coupling between the electrical and chiral charge. The second length is the chiral charge diffusion length $L_c = (D/\tau_c)^{1/2}$, where τ_c is the relaxation time of the chiral charge (or the intervalley relaxation time [41]). The third is the length of the sample L_x in the direction of the electrical current. In a weak magnetic field limit determined by the condition $\left(\dfrac{L_c}{L_a}\right) \ll 1$ along with the long sample limit $L_x \gg L_c$, the following holds according to [18]:

$$\Delta\rho_{\text{chiral}} \sim \left(\frac{L_c}{L_a}\right)^2 \sim B^2, \tag{5}$$

since in this case

$$\frac{L_c}{L_a} = \Gamma B \left(\frac{\tau_c}{D}\right)^{1/2} \approx \frac{\hbar e v_F^2}{\varepsilon_F^2}\left(\frac{\tau_c}{\tau}\right)^{\frac{1}{2}} B. \tag{6}$$

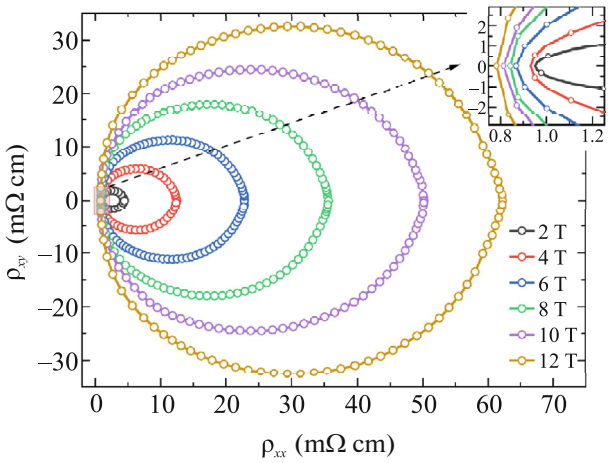

Fig. 3. (Color online) Parametric $\rho_{xy}(\rho_{xx})$ curves in various magnetic fields at $T = 80$ K.

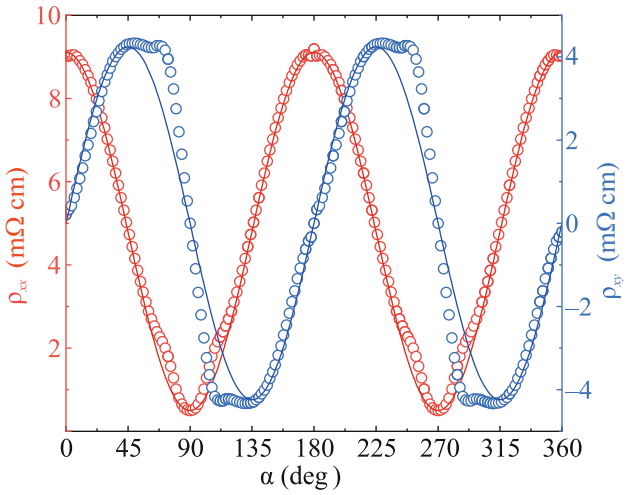

Fig. 4. (Color online) Angular dependence of the planar Hall resistance ρ_{xy} (right axis) and planar longitudinal MR ρ_{xx} (left axis) at $T = 150$ K in the magnetic field of 10 T and their fitting by Eqs. (1) and (2), respectively (solid lines).

Here, $\hbar$ is the reduced Planck constant, τ is the transport relaxation time, and v_F and ε_F are the Fermi velocity and Fermi energy, respectively. In a strong-field limit determined by the condition $\frac{L_c}{L_a} \gg 1$, the amplitude of the PHE should be saturated [18]. The substitution of the electronic parameters of the HgSe sample from [41] into Eq. (6) gives $\left(\frac{L_c}{L_a}\right) \approx 0.35B$. To compare the experimental result with the theory [18], the magnetic field dependence of fitting values $\Delta\rho_{chiral}$ from Fig. 2a is plotted in Fig. 2c with circles. The solid lines represent the fitting of the experimental data by the power law $\Delta\rho_{chiral} \sim B^{\gamma}$. It can be seen that in the region $B \leq 4$ T, where $\frac{L_c}{L_a} \lesssim 1$, the experimental data are well described by the dependence $\Delta\rho_{chiral} \sim B^{1.8}$, which is close to the theoretically predicted one. The dependence $\Delta\rho_{chiral}(B)$ in the region 6 T $\leq B \leq$ 12 T $\left(2 \lesssim \frac{L_c}{L_a} \lesssim 4\right)$ is close to linear. According to the numerically calculated dependence of $\Delta\rho_{chiral}$ on $\frac{L_c}{L_a}$ [18], this magnetic field region is presumably transient from a weak to a strong magnetic field limit, which is inaccessible in this experiment. In topological semimetals such as $ZrTe_{5-\delta}$ [22], Cd_3As_2 [26], $PtTe_2$ [28], T_d-$MoTe_2$ [31], and WTe_2 [32], the magnetic field dependence $\Delta\rho_{chiral}(B)$ in a low magnetic field also obeys a similar power law with the exponent $\gamma \approx 1.8$–2.0 and does not saturate in an experimentally achieved magnetic field. It should be noted that in all of these works the PHE was attributed to the chiral anomaly. Thus, the detected in ultra-pure HgSe PHE is generally is consistent with the theory [18]. The presence of the chiral anomaly in HgSe is confirmed independently by means of the simultaneous observation of a non-saturating negative longitudinal MR (Fig. 2d) together with the PHE. It is remarkable that in addition to this negative longitudinal MR observed in the magnetic field parallel to the electrical current a large positive non-saturating MR is observed in the magnetic field perpendicular to the electrical current, which increases by a factor of about 70 in the magnetic field of 12 T (Fig. 2e). Note that the coexistence of the negative MR at $\mathbf{B} \parallel \mathbf{J}$ and the large positive MR at $\mathbf{B} \perp \mathbf{J}$ seem to be a common feature in Weyl semimetals [47–51], to which HgSe suggestively belongs.

The data presented in Figs. 2a and 2b can be tied together by plotting the parametric $\rho_{xy}(\rho_{xx})$ curves at a fixed magnetic field B using the rotation angle α as a parameter. A set of such parametric curves is shown in Fig. 3. It can be seen that these parametric curves are closed convex nested graphs stretched to the right along the ρ_{xx} axis. It is clear that this stretch along the ρ_{xx} axis reflects the increase in $\rho_{\perp}$ with B (Fig. 2e). Such arrangement of parametric curves is characteristic of topological semimetals, in which the PHE originates from the chiral anomaly [29, 33]. The arrangement of parametric graphs in a solid where the PHE is due to the anisotropy of the orbital MR is different: closed convex curves intersect with each other and shifts noticeably to the right along the ρ_{xx} axis with increasing B [24, 34, 35, 52], which reflects the absence of the negative MR $\rho_{\parallel}(B)$ in the system.

The magnitude of the PHE at $T = 80$ K is of particular interest. The amplitude of the PHE in ultra-pure HgSe reaches an extremely large value of about

50 mΩ cm in the magnetic field of 10 T (Fig. 2a), which exceeds the amplitude of the PHE in other topological semimetals [22–35, 52] by factors of 10–1000 at close temperature and magnetic field. Consequently, the PHE we detected in ultra-pure HgSe can be labled as giant. According to Fig. 2b (right axis), the maximum value of normalized MR in our sample is approximately 7000%, whereas the normalized MR in other topological materials is in the range of 25–500% [22, 25, 27, 34, 35]. With an increase in the temperature from 80 to 150 K, the amplitude of the PHE at $B = 10$ T decreases by a factor of 5.5 to about 9 mΩ cm (Fig. 4) and the maximum value of normalized MR decreases to approximately 1500%. The extremely large magnitude of the PHE in HgSe allows for the application of single HgSe crystals as magnetic sensors susceptible to the in-plane magnetic field component.

CONCLUSIONS

In summary, the discovery of the theoretically predicted PHE in ultra-pure single HgSe crystal combined with the detection in our previous work of the chiral magnetic effect is a solid argument to support the existence of the electronic topological Weyl semimetal phase in this isotropic nonmagnetic material.

FUNDING

This work was supported by the Ministry of Science and Higher Education of the Russian Federation (project no. 075-15-2020-797 (13.1902.21.0024) dated September 29, 2020).

CONFLICT OF INTEREST

The authors declare that they have no conflicts of interest.

OPEN ACCESS

REFERENCES

1. C. Goldberg and R. E. Davis, Phys. Rev. **94**, 1121 (1954).
2. Y. You, Y. Gong, H. Li, Z. Li, M. Zhu, J. Tang, E. Liu, Y. Yao, G. Xu, F. Xu, and W. Wang, Phys. Rev. B **100**, 134441 (2019).
3. K. M. Seemann, F. Freimuth, H. Zhang, S. Blügel, Y. Mokrousov, D. E. Bürgler, and C. M. Schneider, Phys. Rev. Lett. **107**, 086603 (2011).
4. Y. Liu, J. Yang, W. Wang, H. Du, W. Ning, L. Ling, W. Tong, Z. Qu, G. Cao, Y. Zhang, and M. Tian, Phys. Rev. B **95**, 161103 (2017).
5. J. Li, S. L. Li, Z. W. Wu, S. Li, H. F. Chu, J. Wang, Y. Zhang, H. Y. Tian, and D. N. Zheng, J. Phys.: Condens. Matter **22**, 146006 (2010).
6. H. X. Tang, R. K. Kawakami, D. D. Awschalom, and M. L. Roukes, Phys. Rev. Lett. **90**, 107201 (2003).
7. D. Thompson, L. Romankiw, and A. Mayadas, IEEE Trans. Magn. **11**, 1039 (1975).
8. Y. Bason, L. Klein, J.-B. Yau, X. Hong, J. Hoffman, and C. H. Ahn, J. Appl. Phys. **99**, 08R701 (2006).
9. F. N. V. Dau, A. Schuhl, J. R. Childress, and M. Sussiau, Sens. Actuators, A **53**, 256 (1996).
10. S. M. Young, S. Zaheer, J. C. Y. Teo, C. L. Kane, E. J. Mele, and A. M. Rappe, Phys. Rev. Lett. **108**, 140405 (2012).
11. Z. Wang, Y. Sun, X.-Q. Chen, C. Franchini, G. Xu, H. Weng, X. Dai, and Z. Fang, Phys. Rev. B **85**, 195320 (2012).
12. Z. Wang, H. Weng, Q. Wu, X. Dai, and Z. Fang, Phys. Rev. B **88**, 125427 (2013).
13. S.-M. Huang, S.-Y. Xu, I. Belopolski, C.-C. Lee, G. Chang, B. K. Wang, N. Alidoust, G. Bian, M. Neupane, C. Zhang, S. Jia, A. Bansil, H. Lin, and M. Z. Hasan, Nat. Commun. **6**, 7373 (2015).
14. H. Weng, C. Fang, Z. Fang, B. A. Bernevig, and X. Dai, Phys. Rev. X **5**, 011029 (2015).
15. S.-Y. Xu, I. Belopolski, N. Alidoust, et al., Science (Washington, DC, U. S.) **349**, 613 (2015).
16. B. Q. Lv, H. M. Weng, B. B. Fu, X. P. Wang, H. Miao, J. Ma, P. Richard, X. C. Huang, L. X. Zhao, G. F. Chen, Z. Fang, X. Dai, T. Qian, and H. Ding, Phys. Rev. X **5**, 031013 (2015).
17. A. A. Burkov, Nat. Mater. **15**, 1145 (2016).
18. A. A. Burkov, Phys. Rev. B **96**, 041110 (2017).
19. S. Nandy, G. Sharma, A. Taraphder, and S. Tewari, Phys. Rev. Lett. **119**, 176804 (2017).
20. H. B. Nielsen and M. Ninomiya, Phys. Lett. B **130**, 389 (1983).
21. T. D. C. Bevan, A. J. Manninen, J. B. Cook, J. R. Hook, H. E. Hall, T. Vachaspati, and G. E. Volovik, Nature (London, U.K.) **386**, 689 (1997).
22. P. Li, C. H. Zhang, J. W. Zhang, Y. Wen, and X. X. Zhang, Phys. Rev. B **98**, 121108 (2018).
23. S. Xu, H. Wang, X.-Y. Wang, Y. Su, P. Cheng, and T.-L. Xia, arXiv: 1811.06767 (2018).
24. Sonika, M. K. Hooda, S. Sharma, and C. S. Yadav, Appl. Phys. Lett. **119**, 261904 (2021).
25. H. Li, H.-W. Wang, H. He, J. Wang, and S.-Q. Shen, Phys. Rev. B **97**, 201110 (2018).
26. M. Wu, G. Zheng, W. Chu, Y. Liu, W. Gao, H. Zhang, J. Lu, Y. Han, J. Zhou, W. Ning, and M. Tian, Phys. Rev. B **98**, 161110 (2018).

27. R. Singha, S. Roy, A. Pariari, B. Satpati, and P. Mandal, Phys. Rev. B **98**, 081103(R) (2018).
28. A. Vashist, R. K. Singh, N. Wadehra, S. Chakraverty, and Y. Singh, arXiv: 1812.06485 (2018).
29. S. Liang, J. Lin, S. Kushwaha, J. Xing, N. Ni, R. J. Cava, and N. P. Ong, Phys. Rev. X **8**, 031002 (2018).
30. N. Kumar, S. N. Guin, C. Felser, and C. Shekhar, Phys. Rev. B **98**, 041103 (2018).
31. F. C. Chen, X. Luo, J. Yan, Y. Sun, H. Y. Lv, W. J. Lu, C. Y. Xi, P. Tong, Z. G. Sheng, X. B. Zhu, W. H. Song, and Y. P. Sun, Phys. Rev. B **98**, 041114 (2018).
32. P. Li, C. Zhang, Y. Wen, L. Cheng, G. Nichols, D. G. Cory, G.-X. Miao, and X.-X. Zhang, Phys. Rev. B **100**, 205128 (2019).
33. Q. R. Zhang, B. Zeng, Y. C. Chiu, et al., Phys. Rev. B **100**, 115138 (2019).
34. Q. Liu, F. Fei, B. Chen, X. Bo, B. Wei, S. Zhang, M. Zhang, F. Xie, M. Naveed, X. Wan, F. Song, and B. Wang, Phys. Rev. B **99**, 155119 (2019).
35. Z. Li, T. Xiao, R. Zou, J. Li, Y. Zhang, Y. Zeng, M. Zhou, J. Zhang, and W. Wu, J. Appl. Phys. **127**, 054306 (2020).
36. D. E. Kharzeev, Prog. Part. Nucl. Phys. **75**, 133 (2014).
37. B. Z. Spivak and A. V. Andreev, Phys. Rev. B **93**, 085107 (2016).
38. A. A. Burkov, Phys. Rev. B **91**, 245157 (2015).
39. Q. Li, D. E. Kharzeev, C. Zhang, Y. Huang, I. Pletikosi, A. V. Fedorov, R. D. Zhong, J. A. Schneeloch, G. D. Gu, and T. Valla, Nat. Phys **12**, 550 (2016).
40. A. Sekine, D. Culcer, and A. H. MacDonald, Phys. Rev. B **96**, 235134 (2017).
41. A. T. Lonchakov and S. B. Bobin, J. Phys.: Condens. Matter **35**, 065501 (2023).
42. A. T. Lonchakov, S. B. Bobin, V. V. Deryushkin, V. I. Okulov, T. E. Govorkova, and V. N. Neverov, Appl. Phys. Lett. **112**, 082101 (2018).
43. S. B. Bobin, A. T. Lonchakov, V. V. Deryushkin, and V. N. Neverov, J. Phys.: Condens. Matter **31**, 115701 (2019).
44. A. T. Lonchakov, S. B. Bobin, V. V. Deryushkin, and V. N. Neverov, J. Phys.: Condens. Matter **31**, 405706 (2019).
45. C. R. Whitsett, Phys. Rev. A **138**, 829 (1965).
46. I. M. Tsidilkovski, *Electron Spectrum of Gapless Semiconductors* (Springer, Berlin, 1996).
47. C.-L. Zhang, S.-Y. Xu, I. Belopolski, et al., Nat. Commun. **7**, 10735 (2016).
48. X. Huang, L. Zhao, Y. Long, P. Wang, D. Chen, Z. Yang, H. Liang, M. Xue, H. Weng, Z. Fang, X. Dai, and G. Chen, Phys. Rev. X **5**, 031023 (2015).
49. C. Shekhar, A. K. Nayak, Y. Sun, et al., Nat. Phys. **11**, 645 (2015).
50. Z. Wang, Y. Zheng, Z. Shen, Y. Lu, H. Fang, F. Sheng, Y. Zhou, X. Yang, Y. Li, C. Feng, and Z.-A. Xu, Phys. Rev. B **93**, 121112 (2016).
51. J. Du, H. Wang, Q. Chen, Q. H. Mao, R. Khan, B. J. Xu, Y. X. Zhou, Y. N. Zhang, J. H. Yang, B. Chen, C. M. Feng, and M. H. Fang, Sci. China Phys. Mech. Astron. **59**, 657406 (2016).
52. W. Gao, M. Han, Z. Chen, A. Zhu, Y. Han, M. Zhu, X. Zhu, and M. Tian, Appl. Phys. Lett. **122**, 173102 (2023).